Article

Influence of Nickel Doping on Ultrahigh Toluene Sensing Performance of Core-Shell ZnO Microsphere Gas Sensor

Zhenhua Li [1], Sijia Li [1], Zijian Song [1], Xueli Yang [1,*], Ziyan Wang [1], Hao Zhang [2], Lanlan Guo [3], Caixuan Sun [1], Hongyan Liu [1], Junkai Shao [1], Yehong Cheng [4,*] and Guofeng Pan [1]

[1] Tianjin Key Laboratory of Electronic Materials and Devices, School of Electronics and Information Engineering, Hebei University of Technology, 5340 Xiping Road, Beichen District, Tianjin 300401, China
[2] Tianjin Key Laboratory of Materials Laminating Fabrication and Interface Control Technology, School of Materials Science and Engineering, Hebei University of Technology, Tianjin 300130, China
[3] School of Physics and Electronic Information Engineering, Henan Polytechnic University, Jiaozuo 454003, China
[4] School of Mechanical Engineering, Hebei University of Technology, Tianjin 300401, China
*   Correspondence: xlyang@hebut.edu.cn (X.Y.); chengyehong@hebut.edu.cn (Y.C.)

Abstract: As a volatile organic compound, toluene is extremely harmful to the environment and human health. In this work, through a simple one-step solvothermal method, Ni-doped ZnO sensitive materials (0.5, 1, and 2 at% Ni-doped ZnO) with a core-shell morphology were synthesized for the first time for toluene gas detection. The sensing test results showed that the sensor based on 1 at% Ni-doped ZnO exhibited the best toluene sensing performance. The response was up to 210 to 100 ppm toluene at 325 °C. The sensor exhibited high selectivity, fast response/recovery characteristics (2/77 s), and low detection limit (500 ppb, 3.5). Furthermore, we carried out molecular-level research on the sensitive material prepared in this experiment by various characterization methods. The SEM characterization results showed that ZnO and Ni-doped ZnO possessed the core-shell morphology, and the average grain size decreased with the increase in the Ni doping content. The UV–Vis test showed that the band gap of ZnO became smaller with the increase in the Ni doping amount. The enhanced toluene sensing performance of 1 at% Ni-doped ZnO could be ascribed to the structural sensitization and Ni doping sensitization, which are discussed in detail in the sensing mechanism section.

Keywords: Ni doping; ZnO; gas sensor; toluene; core-shell structure

1. Introduction

With the development of modern industry, various kinds of poisonous and harmful gases have been produced, which will cause harm to human health and the environment. In particular, volatile organic compounds (VOCs) such as ethanol, acetone, formaldehyde, and toluene, etc., which widely exist in our surroundings. Among them, toluene as a typical aromatic compound is a kind of colorless gas with a special fragrance, and is widely used in many aspects of production and life such as raw materials in the chemical industry, the production of dyes, pharmaceuticals, pesticides, explosives, and other fine chemicals. In addition, it can be used as a food preservative in major food production factories [1]. Meanwhile, toluene is a flammable and harmful gas and can produce an anesthetic effect on the central nervous system, causing great and irreparable harm to the human body. Therefore, toluene has been identified as a highly toxic carcinogen by the International Center for Research on Cancer [2]. Due to the harmfulness of toluene, it is very necessary and urgent to develop a high performance toluene gas sensor to monitor toluene in real-time to ensure human health and environmental safety.

Gas sensors based on semiconductor metal oxides have attracted extensive attention in recent years due to their advantages of high sensitivity, easy fabrication, low cost, and small

size. As the most promising sensing material, gas sensors based on semiconductor metal oxides have become a research hotspot. Up to now, many metal oxide semiconductors have been developed and used as gas sensing materials, for instance, ZnO [3,4], In_2O_3 [5–7], SnO_2 [8–10], WO_3 [11–13], NiO [14,15], CuO [16,17], etc. Among the n-type and p-type single semiconductor oxides, ZnO is the most widely studied gas sensing material as ZnO is an n-type semiconductor oxide with a wide band gap energy (3.37 eV) and a large excite binding energy (60 MeV) [18,19]. The physical and chemical properties of ZnO are stable, and the electrical property of ZnO is tunable with transition metal doping [20]. Currently, different morphologies of ZnO have been reported to detect different gases [21–27] including nanoparticles [28], one-dimensional nanowires [29], nanorods and nanofibers, two-dimensional nanosheets [30], nanoribbons and nanorings as well as three-dimensional flower-like structures [31], core-shell structures, and hollow spheres. Studies have shown that the hierarchical structure of ZnO enables better gas sensing properties due to its larger specific surface area, porosity, and permeability.

In addition to constructing the hierarchical structure of ZnO, it is also an effective way to improve the gas sensitive performance by doping. There are many types of doping substances including metal oxides, precious metals, transition metals, carbon-based materials, and polymers [32–36]. Since transition metal ions can be doped into the semiconductor lattice, the lattice distortion of sensitive materials generates a large number of defects and vacancies. The increase in the defect concentration on the surface can improve the adsorption of oxygen anions on the surface of the material, thereby improving the gas-sensing response value of the sensing material. Thus far, many studies have reported that through transition metal doping, improved gas sensing performance can be achieved. Transition metal doping elements including Co, Sn, Fe, and Ni [37–40] etc. have been reported to tune the sensing performance of ZnO. The catalytic properties, surface properties, and charge carriers of pristine semiconductor materials can be improved by doping transition metal elements. Guo [41] et al. successfully synthesized Fe-doped ZnO/rGO nanocomposites via a simple hydrothermal process. The sensor exhibited a response of 12.7 to 5 ppm formaldehyde at 120 °C. Compared with pure ZnO, the response of the doped sensing material was about 3 times higher. The reason for the enhanced sensing performance is that the doping of Fe changes the band gap, making the band gap of ZnO smaller and generating a large number of oxygen vacancies.

Based on that demonstrated above, the gas sensing performance of semiconductor metal oxides can be improved by constructing a hierarchical structure to adjust the surface area and doping transition metal elements to tune the electrical and catalytic properties [42–44]. To our best knowledge, fabricating a core-shell Ni doped ZnO (Ni–ZnO) to achieve an enhanced sensing performance of toluene has rarely been reported.

Here, materials with different ratios of 0, 0.5, 1, and 2 at% Ni–ZnO core-shell morphologies were successfully prepared by a simple solvothermal method and used for toluene gas detection. Gas sensing measurements showed that out of all the four gas sensors, the sensor based on 1 at% Ni–ZnO had the highest toluene response of 210 (100 ppm, 325 °C), which was almost seven times higher than pure ZnO (33.6, 375 °C). Moreover, the sensor also had high selectivity, low detection limit, and fast response/recovery properties. The sensing mechanism of the enhanced sensing properties was analyzed in detail.

2. Materials and Methods

2.1. Synthesis of the Pure ZnO and Ni–ZnO Core-Shell Spheres

First, 20 mL of deionized water and 1 mmol Ni $(CH_3COO)_2 \cdot 4H_2O$ were added into a 50 mL beaker and stirred for 20 min. Then, 7 mL of glycerol and 30 mL of isopropanol were added into a 50 mL beaker with vigorous stirring, and 0.45 mmol Zn $(CH_3COO)_2 \cdot 2H_2O$ was dissolved into the above mixed solution with stirring for 15 min, named as solution A. Then 0, 45, 90, and 180 μL of the above prepared Ni $(CH_3COO)_2 \cdot 4H_2O$ solution were added into solution A, respectively, and stirring was continued for another 20 min. Then, the four solutions were placed in an oven and kept at 180 °C for 24 h. After the reaction was

completed, the temperature was naturally cooled to room temperature, and the product was separated by centrifugation, alternately washed with anhydrous ethanol and deionized water, and then dried at 80 °C for 10 h. The dried product was calcined at 500 °C for 2 h (heating rate, 2 °C·min^{-1}). Finally, pure ZnO and 0.5, 1, and 2 at% Ni–ZnO core-shell products were obtained.

2.2. Characterization

In this paper, an X-ray powder diffractometer (XRD; Bruker D8 Discover, Billerica, MA, USA) was used to investigate the composition and crystallinity of pure ZnO and different proportions of the Ni–ZnO samples. Diffraction analysis of sensitive materials was carried out using Cu Kα1 rays (λ = 1.5406 Å) in the range of 2θ from 20 to 80°, and the scanning step was 10°·min^{-1}. The microscopic topography of sensitive materials can be analyzed and studied using scanning electron microscopy (SEM; ZEISS Sigma 500, Jena, Germany). More information about the microscopic morphology and the lattice size of sensitive materials can be obtained by transmission electron microscopy and high-resolution transmission electron microscopy. In addition, energy dispersive X-ray spectrometry (EDS) enables the detection of element mapping distributions. The chemical element analysis was obtained from the X-ray photoelectron spectroscopy (XPS; Escalab 250 XI, Waltham, MA, USA) measurements, and the surface area and pore size distribution were calculated by the Brunauer–Emmett–Teller (BET) and Barrett–Joyner–Halenda (BJH) methods using the nitrogen adsorption–desorption isotherm test (Micromeritics ASAP2000 system, USA). The absorbance and band gap of the sample were measured by using a UV–Visible spectrophotometer (UV–Vis; Lambda 1050+, Waltham, MA, USA) between 250 and 800 nm.

2.3. Fabrication and Measurement Process of the Gas Sensors

As schematically shown in Figure S1a,b, first, the as-synthesized sample (3–5 mg) and an appropriate amount (0.3–0.5 mL) of deionized water were mixed to form a slurry. Then, the slurry was evenly coated on the surface of the ceramic tube (outer diameter 1.2 mm, inner diameter 0.8 mm, length 4 mm) using a small brush. After drying in air for 15 min, the ceramic tube was placed in a Muffle furnace at 400 °C for 120 min with a heating rate of 2 °C min^{-1} to enhance the stability during the test process. After that, a Ni–Cr alloy wire, which provides the operating temperature by tuning the constant current, is inserted in the sintered ceramic tube. Finally, the sensor was welded on a six-legged sensor base, and the gas sensing performance was tested after aging for 24 h with 100 mA. Figure S1c is schematically shown as the static gas sensing test system. A constant-current power (Gwinstek GPD-3303S, New Taipei City, Taiwan) was used to supply a constant current for the Ni–Cr alloy wire to control the operating temperature. Two glass cavities with a volume of 1 L were used to hold air and test gas, respectively. A digital multimeter (Fluke 8846a, Everett, WA, USA) and a computer was used to record and monitor the resistance of the gas sensor. During the sensing test process, the sensor was alternately placed in 1 L of fresh air in the glass cavity for a few minutes to obtain a stabilized resistance value recorded as Ra. Then, the gas sensor device was transferred to another glass cavity with 1 L, which was filled with a mixture of fresh air and target gas, the stabilized resistance value in the target gas was recorded as Rg. The sensing test was carried out in a laboratory environment (25 °C, 30 RH%). The volatile organic gas used was an analytical grade liquid, and injected to the glass cavity by a microinjector. The gas preparation process is detailed in the Supplementary Materials. The gas sensing response was defined as S = Ra/Rg, and response/recovery time was the time taken by the sensor to reach 90% of the overall resistance change.

3. Results

The XRD pattern of the pure ZnO, 0.5, 1, and 2 at% Ni–ZnO core-shell spheres are shown in Figure 1a. The diffraction peaks appeared at 34.42°, 36.25°, 47.53°, 56.60°, 62.85°, 68.17°, 69.29°, which corresponded to the (100), (002), (101), (102), (110), (103), and (112)

crystal planes of the hexagonal wurtzite phase ZnO (JCPDS No. 36-1451) [45]. However, no peak matched with Ni or NiO in the Ni–ZnO samples. No other diffraction peaks corresponding to the impurities were detected. Figure 1b is the high-resolution peak of the (101) plane of ZnO compared to pure ZnO, and the diffraction peak of Ni–ZnO shifted to a higher angle direction. The shift of 2 at% Ni–ZnO sample was the most obvious, which indicated that Ni^{2+} was incorporated in the ZnO crystal lattice due to the radius of Ni^{2+} being smaller than Zn^{2+}.
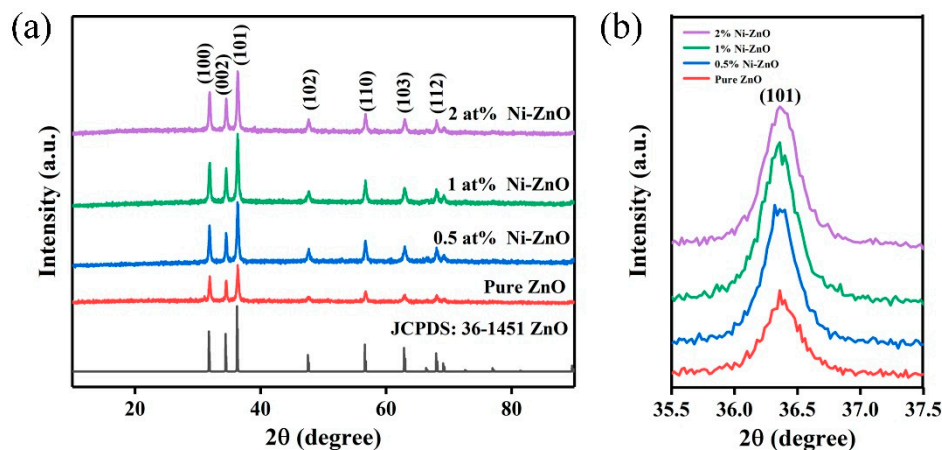

Figure 1. (**a**) The XRD patterns of the pure and Ni–ZnO, (**b**) enlarged spectra of the XRD patterns of the Ni–ZnO.

Figure 2a–d shows the SEM images of the 0, 0.5, 1, and 2 at% Ni–ZnO sample, respectively. The pure ZnO, 0.5, and 1 at% Ni–ZnO samples showed a core-shell spherical hierarchical structure, and there was no obvious core-shell structure observed for 2 at% Ni–ZnO; the morphology was a simple spherical structure. It was found from the SEM images that with the increase in the Ni doping content, the surface of the ZnO microspheres became more and more coarse and the average particle size of the spheres decreased. The average particle size was 15.10, 9.42, 5.62, and 4.66 μm for pure ZnO, 0.5, 1 and 2 at% Ni–ZnO spheres, which suggests that the addition of Ni ions can inhibit the growth of ZnO particles in the hydrothermal reaction process. In addition, the inserted magnified SEM images showed that the core of the core-shell spheres was very large and next to the shell. Proper Ni doping, a rough surface, and loose shell are favorable for gas adsorption and diffusion, with a high gas sensing performance, which will be verified in later sections.

Figure 3a,b are TEM images of different magnifications, whose shape and size are consistent with the SEM characterization results. The inset figure is the selected area electron diffraction (SAED) image and shows that the 1 at% Ni–ZnO sample had a polycrystalline structure. Figure 3c is the HRTEM images of the 1 at% Ni–ZnO sample. The lattice spacings were 0.286 and 0.249 nm, corresponding to the (100) and (101) crystal planes of ZnO [46,47]. Interplanar spacing corresponding to NiO was not found, which is consistent with the results of the XRD. From the element mapping test results in Figure 3d–g, the three elements (Ni, O, and Zn) were evenly distributed in the 1 at% Ni–ZnO sample.

The specific surface area of the pure ZnO and Ni–ZnO samples was determined by the nitrogen adsorption/desorption isotherm. As illustrated in Figure 4a–e, the adsorption–desorption curve is an iv-type isotherm belonging to the H3 hysteresis loop, indicating that Ni–ZnO has a microporous structure [48].The specific surface area increased with the increase in the Ni doping amount, especially for 1 and 2 at% Ni–ZnO, the specific surface areas were 20.43 to 26.41, 37.54 and 40.14 $m^2 \cdot g^{-1}$ for the pure ZnO, 0.5, 1, and 2 at% Ni–ZnO. The results showed that with the proper amount of Ni doping, the specific area of ZnO could increase a lot; when the doping amount reached a certain value, the specific area did not increase too much. A large specific area could supply more surface-active sites for

surface adsorbed oxygen species, thus improving the recognition function of the sensing material and contributing to the high gas sensing performance.

Moreover, the inset of Figure 4 shows the nonlocal density functional theory (NLDFT) and grand canonical Monte Carlo (GCMC) pore size distribution of the Ni–ZnO, and through analysis, it was found that the pore sizes of the pure ZnO and 0.5 at%, 1 at%, and 2 at% Ni–ZnO were 46.8, 58.08, 32.72, and 32.71 nm, respectively. Appropriate Ni ion doping can increase the size of the pore size, and combined with the gas sensing data, it can be inferred that the pore size of the sensitive material in this experiment had little effect on the gas sensing performance. The increase in the specific surface area is one of the main factors affecting the gas sensing performance.
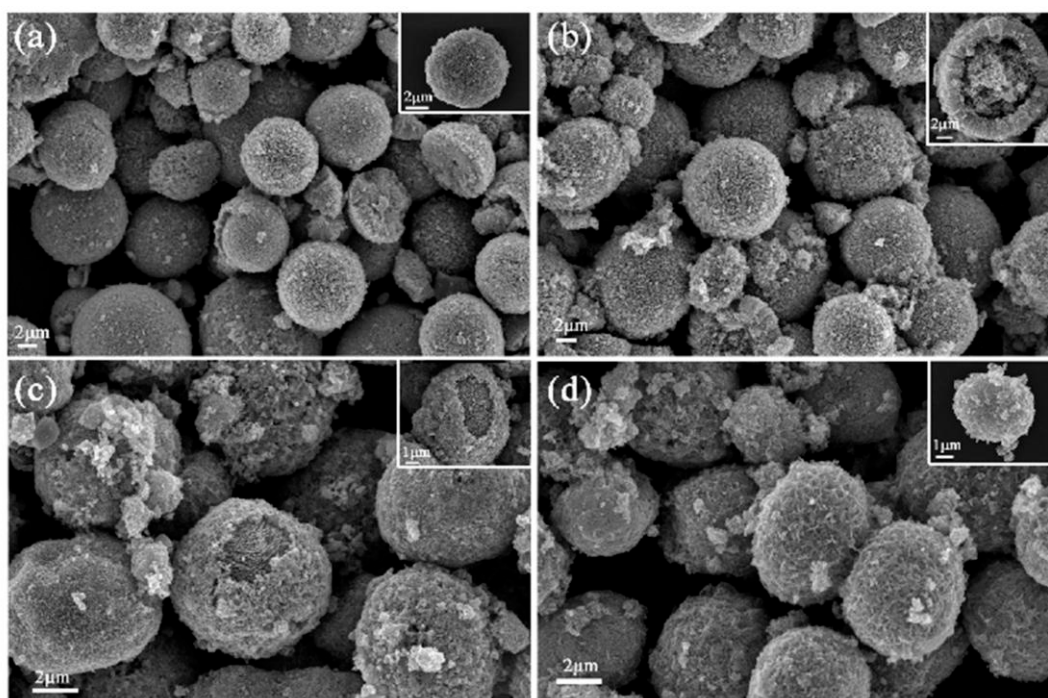

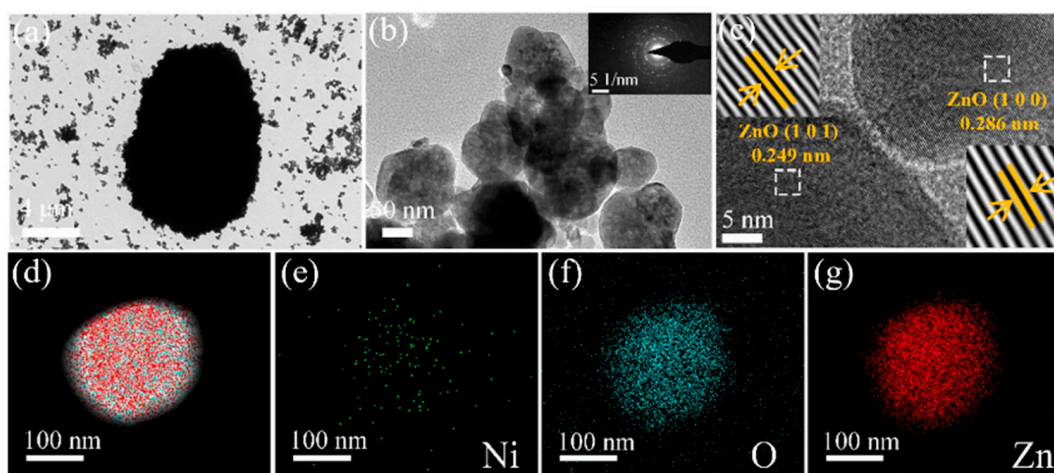**Figure 2.** The SEM images of the (**a**) pure (**b**) 0.5 at% (**c**) 1 at%, and (**d**) 2 at% Ni–ZnO.

Figure 3. The TEM image of 1 at% Ni–ZnO (**a**,**b**). (**c**) HRTEM images of 1 at% Ni–ZnO. (**d**) The overlapped elemental mapping of Ni, O, Zn in the 1 at% Ni–ZnO sample, and (**e**–**g**) elemental mapping of Ni, O, and Zn.
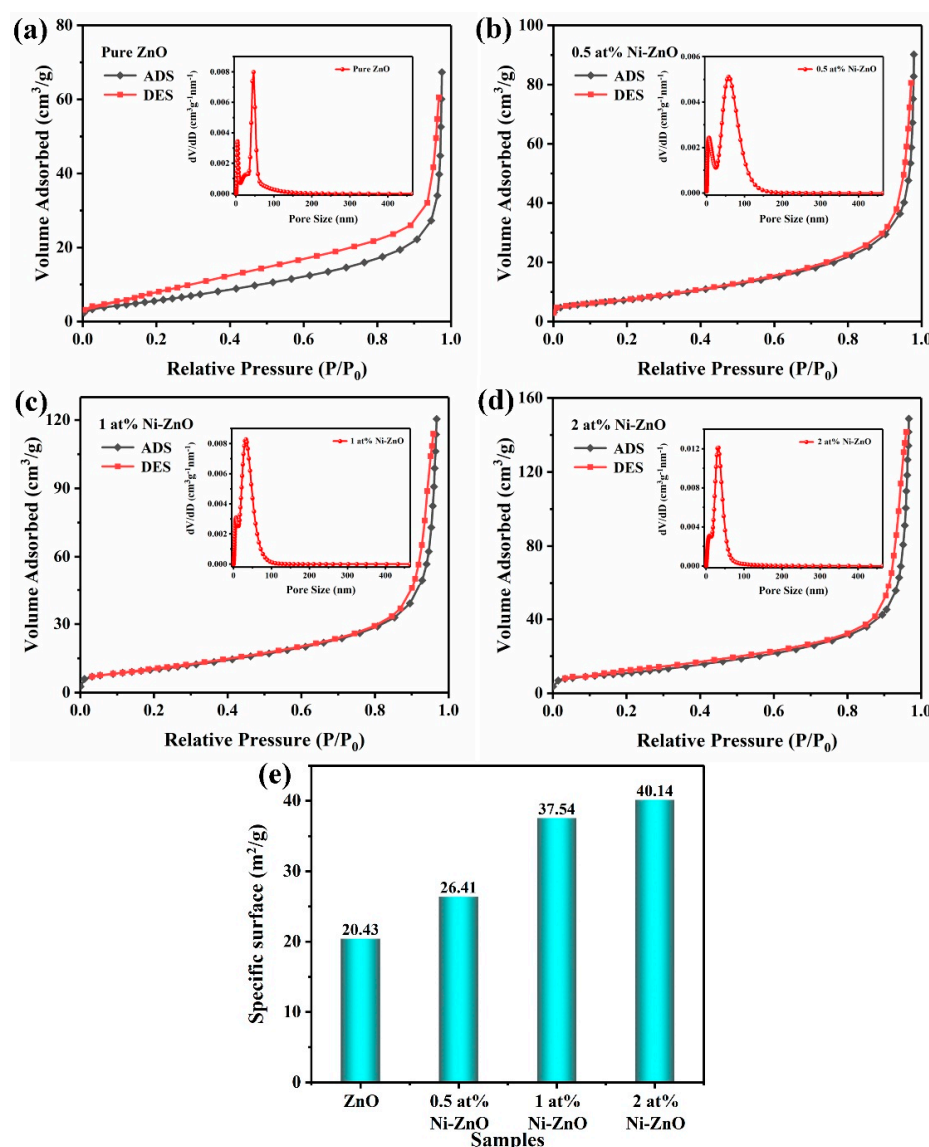
Figure 4. The nitrogen absorption–desorption isotherms and pore size distribution curves (inset) of the (**a**) pure ZnO and (**b**) 0.5 at% (**c**) 1 at%, and (**d**) 2 at% Ni–ZnO. (**e**) Specific surface area of the samples.

The XPS measurement was used to analyze the chemical composition and states of the elements in the pure ZnO and Ni–ZnO samples. Figure 5a exhibits the full spectrum of the ZnO and Ni–ZnO samples, where the full spectrum contained the peaks of Zn, O and Ni, proving the presence of Zn, O, and Ni in the sample. In Figure 5b, the binding energy around 1021.20 and 1044.28 eV corresponded to Zn $2p_{3/2}$ and Zn $2p_{1/2}$, respectively, proving that Zn was in the form of Zn^{2+} [49]. Figure 5c–e shows that the Ni $2p_{3/2}$ orbital can be separated into three peaks of about 854.1, 856.3, and 861.2 eV, corresponding to the Ni^{2+}, Ni^{3+} and satellite peaks, respectively [50], indicating the existence of Ni ions in the ZnO crystals.

Figure 6a–d is the XPS spectra of the O 1s of all samples, the peak shape is asymmetric, and can be allocated into three different oxygen components: chemisorbed gen (O_C), oxygen vacancy (O_V), and lattice oxygen (O_L), which correspond to the peaks at around 532.2 ± 0.5 eV, 531.0 ± 0.5 eV, and 529.5 ± 0.5 eV [51,52], respectively. Table 1 shows the relative proportion of the three oxygen components of O 1s in all of the samples. The relative ratio of O_C did not change a lot, but with Ni doping, the ratio of O_L decreased, while relatively, the proportion of O_V increased, and 1 at% Ni–ZnO showed the highest

proportion of O_V with 22.8%. Ni doping led to the formation of an oxygen vacancy in ZnO, and more O_V concentration distributed to more surface-active sites, thus benefiting more surface negatively charged oxygen species.
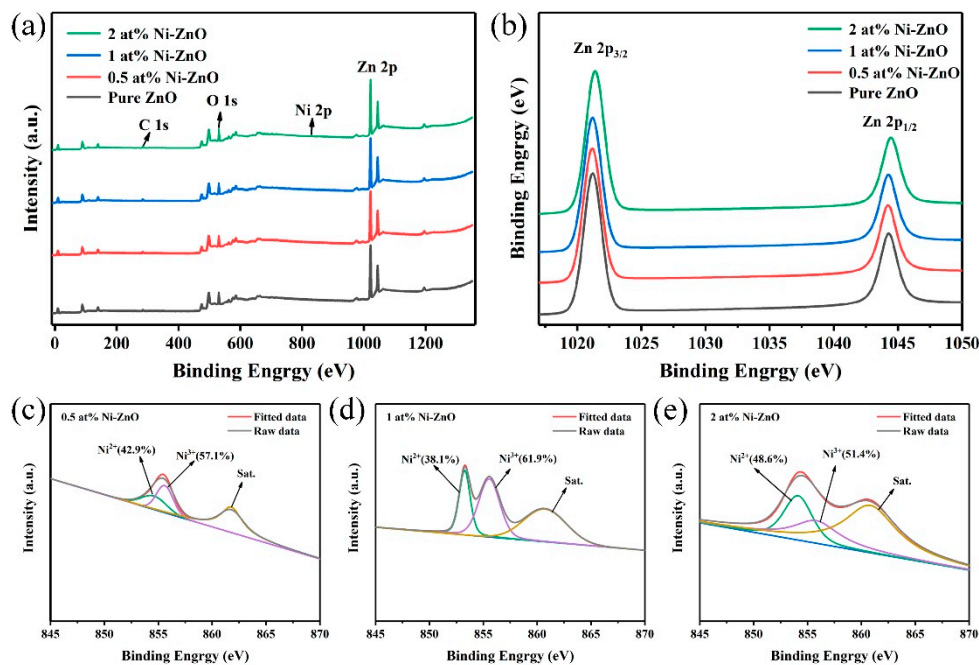

Figure 5. The XPS spectra of the pure and Ni–ZnO for (**a**) the full scan, (**b**) Zn 2p, (**c**–**e**) Ni $2p_{3/2}$ of 0.5, 1, 2 at% Ni–ZnO.
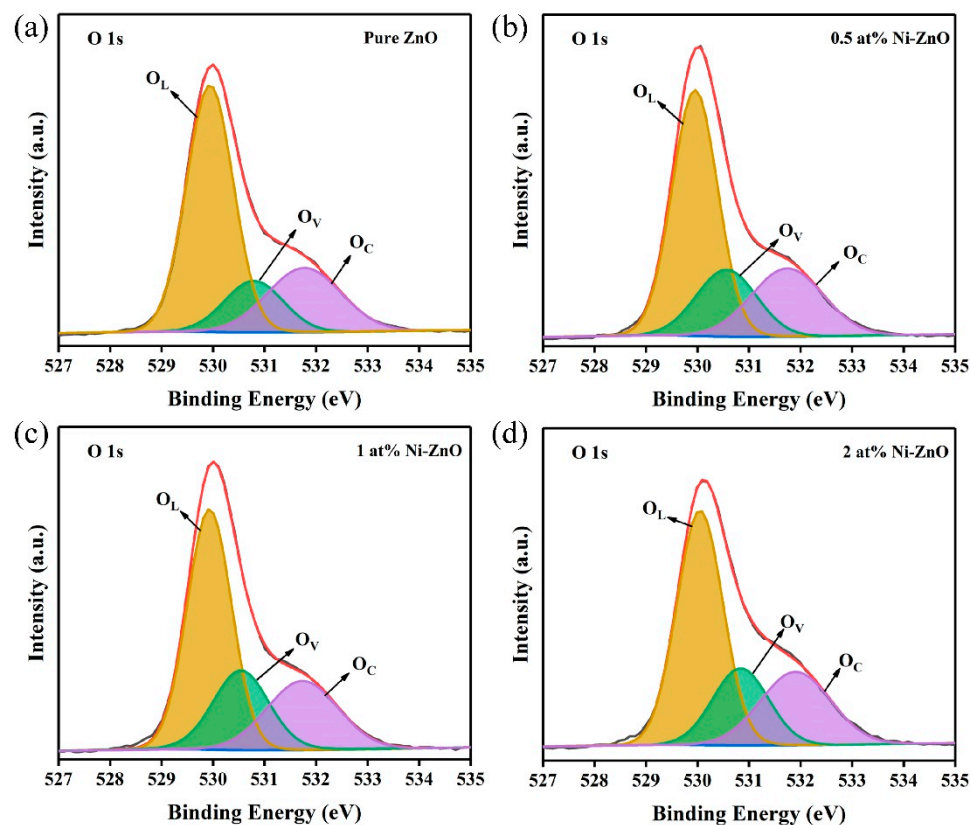

Figure 6. The XPS spectra of O 1s for (**a**–**d**) pure, 0.5, 1, and 2 at% Ni–ZnO.

Table 1. The relative percentages of O 1s in the XPS spectra ZnO, 0.5 at%, 1 at%, and 2 at% Ni–ZnO.

Species	Peak (eV)	ZnO	0.5 at% Ni–ZnO	1 at% Ni–ZnO	2 at% Ni–ZnO
O_L	529.9	60.0%	55.9%	53.0%	53.7%
O_V	530.8	15.6%	19.9%	22.8%	21.0%
O_C	531.7	24.4%	24.2%	24.2%	25.3%

Gas Sensing Characteristics

The operating temperature can affect the carrier concentration and gas adsorption and desorption of the sensor resistance and gas response [53,54]. Response of the four sensors to 100 ppm toluene at different temperatures (Figure 7a) showed that the response values first increased and then decreased. The maximum response values of the four sensors reached at 375 °C (pure ZnO), 350 °C (0.5 at% Ni–ZnO), and 325 °C (1 and 2 at% Ni–ZnO), and the response values were 33.6, 111.4, 210.0 and 23.1, respectively. The 1 at% Ni–ZnO sample had the highest response of 210.0, which was seven times higher than the pure ZnO. With Ni doping, the operating temperature of 1 at% Ni–ZnO was significantly decreased, which could be explained by the change in the band gap, as illustrated in Figure S2. After Ni doping, the band gap reduced from 3.05 to 2.89 eV, and free electrons were easier to release from the conduction band. Figure 7b displays the responses of the four sensors to the six tested target gases (toluene, ethanol, acetone, methanol, formaldehyde, and xylene) with 100 ppm at their optimal operating temperatures (ZnO, 375 °C; 0.5 at% Ni–ZnO, 350 °C; 1 and 2 at% Ni–ZnO, 325 °C). Obviously, the four sensors had the highest response to toluene. Compared with the other tested gases, the 1 at% Ni–ZnO sensor showed the best toluene sensing performance, and the response to toluene and other gases was 210.0, 52.0, 3.4, 9.4, 3.1, and 1.5. The toluene response was 4–140 times higher than other measured gases, indicating that the sensor had excellent selectivity for toluene.
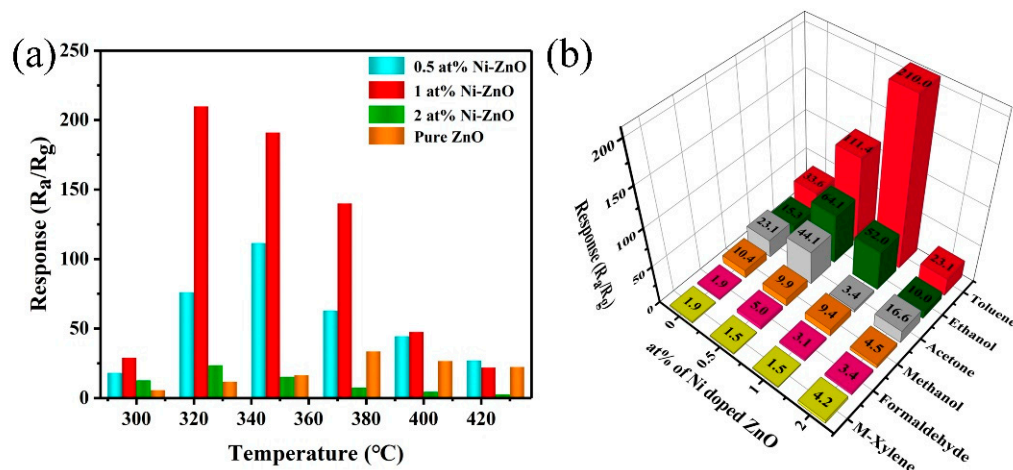

Figure 7. (**a**) The response of the four gas sensors to 100 ppm toluene at different temperatures. (**b**) The selectivity of the four gas sensors to 100 ppm different VOC gases at their optimum operating temperature.

Figure 8a,b shows the real-time response curves of the four sensors at 375 °C (pure ZnO) and 325 °C (Ni–ZnO samples) with different concentrations of toluene. The response value increased with the increase in toluene concentration. The sensor response based on 1 at% Ni–ZnO increased significantly with increasing toluene concentration. The corresponding linear relationship between the toluene response and concentration is listed in Figure 8c,d. It can be observed that the linearity of the sensor was very good in both the low-concentration range and the high-concentration range. The response increased almost linearly with the toluene concentration, and 1 at% Ni–ZnO had the highest sensitivity.

Furthermore, the sensor based on 1 at% Ni–ZnO had a low detection limit of 0.5 ppm with a response value of 3.5, which makes it promising in practical application.
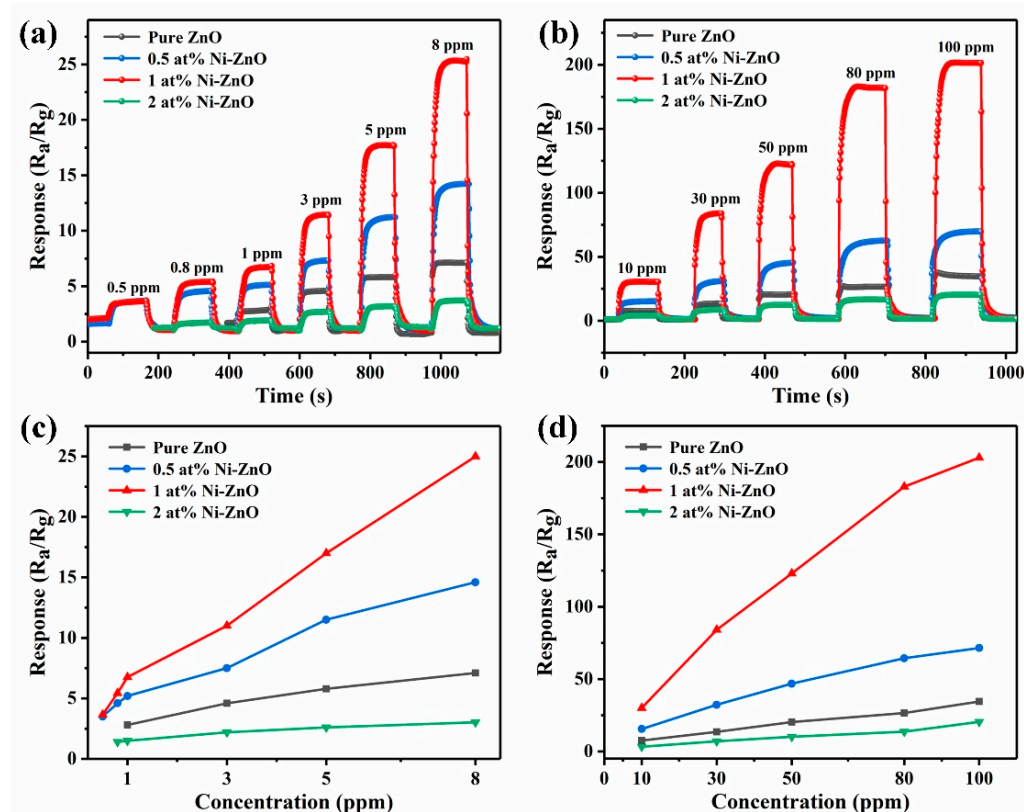

Figure 8. (**a,b**) The dynamic response curves of the four sensors to toluene with different concentrations at 375 °C (pure ZnO) and 325 °C (Ni–ZnO samples). (**c,d**) The response of the pure, 0.5, 1, and 2 at% Ni–ZnO sensors to (0.5–100 ppm) toluene.

The response and recovery characteristics are also important parameters of gas sensors. Thus, the response and recovery transients of the sensor based on 1 at% Ni–ZnO to 100 ppm toluene at 325 °C are shown in Figure 9a. The response time and recovery time of the sensor based on 1 at% Ni–ZnO are 2 and 77 s, respectively, illustrating that the sensor had a relatively fast response and recovery property. Table 2 is a comparison of the toluene sensing performance of this work and the sensors reported in the literature [55–59]. The operating temperature was relatively higher than that in the literature, but the response and recovery time were fast and the toluene response was much higher than the reported literature.

Figure 9b is the resistance in air as a function of operating temperature. With the increase in Ni doping, the resistance of the sensor increased significantly. The resistance versus temperature plot of the sensors showed an abnormal PTCR (positive temperature coefficient of resistance) behavior during 300–350 °C. Based on the reported literature [60], this phenomenon was caused by Ni doping, which introduced defects in ZnO, thus forming oxygen vacancy-like defects in this temperature region.

Figure 9c is a seven-cycle test curve of the 1 at% Ni–ZnO sample to 100 ppm toluene at 325 °C. The resistance in air and toluene was within the allowable fluctuation range, proving that the sensor had good repeatability. The long-term stability was also studied in this work; the sensing response to 100 ppm toluene in the air for one month is shown in Figure 9d. During the test days, the response values varied and slightly decreased but did not show an obvious fluctuation. The results indicate that the 1 at% Ni–ZnO gas sensor has good long-term stability.
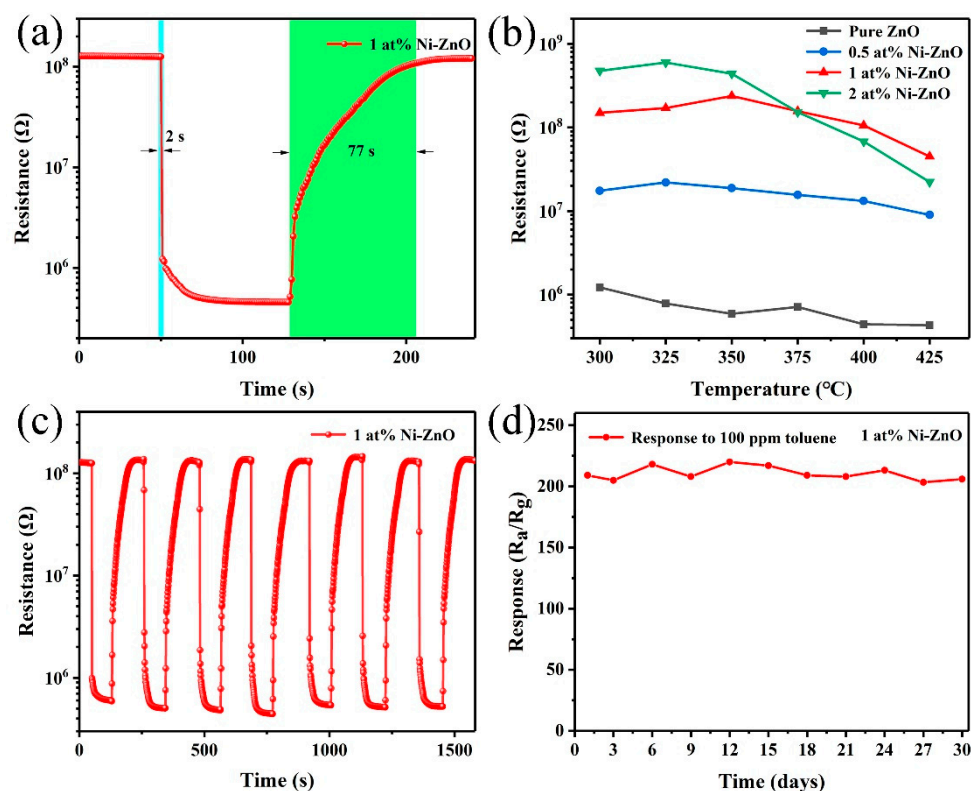
Figure 9. (**a**) The response/recovery time of 1 at% Ni–ZnO gas sensor to 100 ppm toluene at 325 °C. (**b**) Resistance in the air of the four gas sensors at different operating temperatures. (**c**) Seven reversible cycles of 1 at% Ni–ZnO gas sensors. (**d**) The stability testing curves of 1 at% Ni–ZnO gas sensor to 100 ppm toluene in 30 days.

Table 2. A comparison of the toluene gas sensing performance of this work and other sensing material in previously reported works.

Sensing Material	Conc. in ppm	Operating Temperature (°C)	Response	Res/Rec (s)	LOD (ppm)	Ref.
WO_3–SnO_2	10	340	5.6	14.5/406	-	[55]
SnO_2–ZnO	50	200	7.5	90/150	0.1	[56]
$NiGa_2O_4$–NiO	100	230	12.7	60/70	0.5	[57]
NiO/$NiGa_2O_4$	5	200	10.54	600/-	-	[58]
CuO–SnO_2	75	400	540	100/36	10	[59]
Ni–ZnO	100	320	210	2/77	0.5	Present work

4. Discussion

The gas sensing mechanism can be explained by the interaction of multiple factors. In this work, toluene sensing mechanisms with exceptional response are discussed in detail. The gas sensing mechanism has been widely explored in many studies [61,62], and the extensively accepted theory is the chemical reaction between the target gas and chemically adsorbed oxygen species (O_2^- (T < 100 °C), O^- (100 °C < T < 300 °C), and O^{2-} (T > 300 °C)) [63,64]. When redox reactions take place on the surface of the semiconductors, charge transfer will occur during this process, which changes the resistance of the gas sensor.

As illustrated in Figure 10, when the Ni–ZnO gas sensor is exposed to air, O_2 molecules will capture electrons in the conduction band of the material to form negatively charged oxygen species on the surface of the Ni–ZnO material, and a depletion layer will form on the surface at the same time, leading to a high resistance of the sensor in air. Then, when

the sensor is exposed to a reducing gas (toluene) environment, the chemically adsorbed oxygen can react with the target gas molecules on the surface of the sensing material, the electron depletion layer becomes smaller. As a result, electrons that are released back into the conduction band induce lower resistance values in reducing gases. The relevant reactions are seen in Equations (1)–(3) (T > 300 °C) [65]:

$$O_2 \rightarrow O_{2(ads)} \tag{1}$$

$$O_{2(ads)} + 4e \rightarrow 2O^{2-} \tag{2}$$

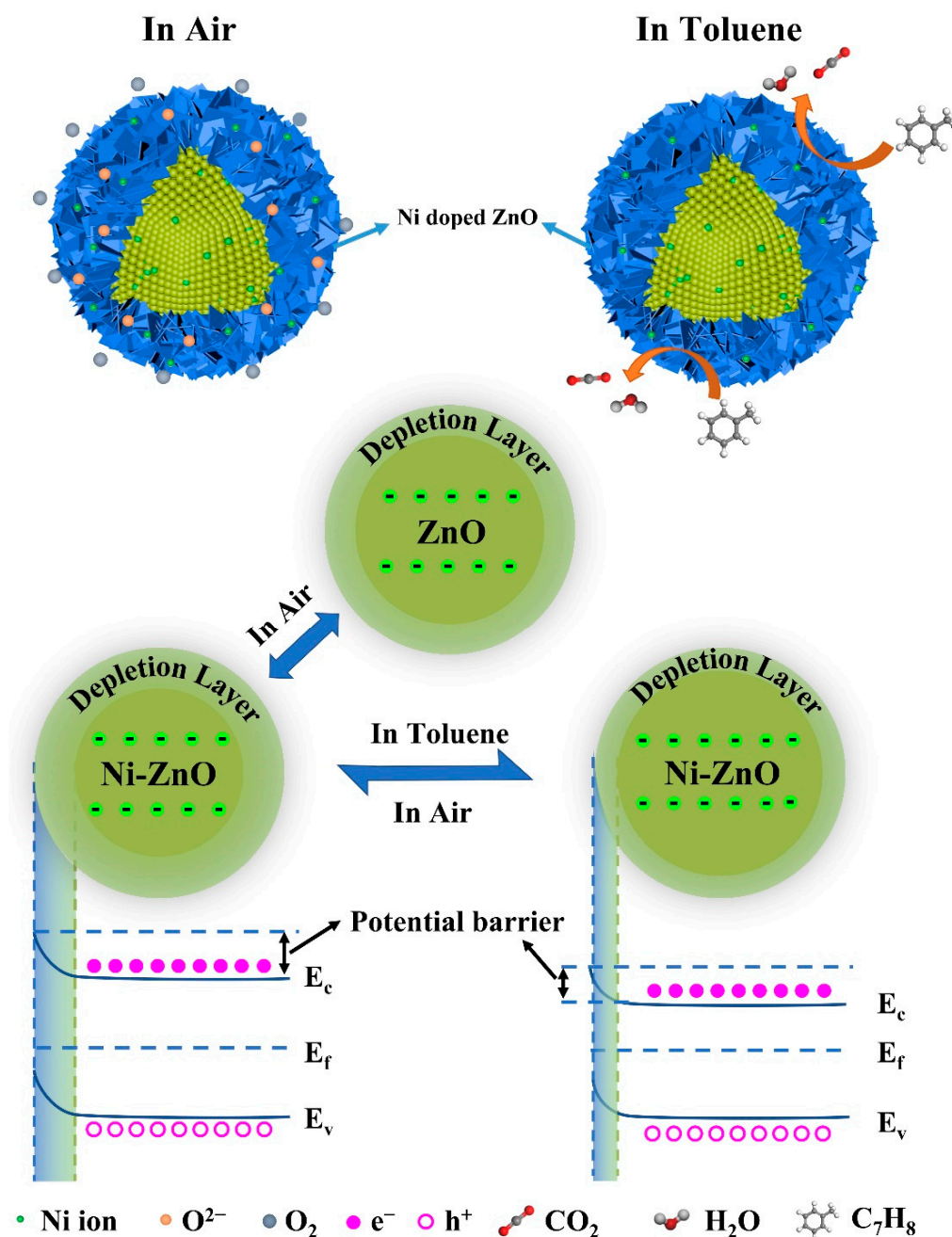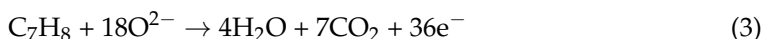$$C_7H_8 + 18O^{2-} \rightarrow 4H_2O + 7CO_2 + 36e^- \tag{3}$$

Figure 10. A schematic diagram of the sensing mechanism.

The enhanced sensing performance of the 1 at% Ni–ZnO-based gas sensor can be attributed to the following two aspects including structural sensitization and modified

sensitization. The first is structural sensitization. After Ni doping, the hierarchical microstructure of ZnO changed, and the surface of the Ni–ZnO core-shell spheres became rougher. This loose structure is very favorable for the diffusion of gas molecules, which can not only penetrate into the shell at the outer surface of the material, but may also further diffuse to the surface of the core. Therefore, the sensing material has a higher sensing performance [66]. Furthermore, the thickness of the shell of the sensing material becomes thinner with increasing Ni content. According to the literature [67,68], when the thickness of the shell layer is close to the Debye length, the gas sensing material has the best gas sensing performance. Finally, the size of the topography of the gas sensing material is also affected by Ni, resulting in a smaller morphology size. An appropriate reduction in the morphology size can lead to an increase in the specific surface area, which can adsorb more oxygen and toluene molecules and provide more active sites [69].

Modified sensitization includes the following points. First, the specific surface area increased with Ni doping, so the recognition function of the sensing material will be improved. Second, it can be seen from Table 2 that Ni doping increased the relative proportion of oxygen vacancy in ZnO. The oxygen vacancy improved from 15.6% to 22.8 for 1 at% Ni–ZnO, which means that more oxygen species will adsorb on the surface of 1 at% Ni–ZnO and the sensing performance will be enhanced. The third and most important point is that Ni^{2+} ions can be easily oxidized into Ni^{3+} with a higher oxidation state, which will facilitate the redox reaction, due to which Ni^{3+} usually plays the role of the catalyst during the redox process, as many studies have reported [70–72]. Therefore, a greater percentage of Ni^{3+} will obtain a good gas sensing property to a large extent. Figure 5c–e displays the fitted XPS results of Ni^{2+} and Ni^{3+} of the 0.5, 1, and 2 at% Ni–ZnO. The relative percentage of Ni^{2+} and Ni^{3+} varied in the three samples, and the ratio of Ni^{3+}/Ni^{2+} was calculated to be 1.33, 1.62, and 1.05 for the 0.5, 1, and 2 at% Ni–ZnO samples. The 1 at% Ni–ZnO sample had the highest ratio of Ni^{3+}/Ni^{2+} of 1.62, followed by the 0.5 at% Ni–ZnO and 2 at% Ni–ZnO. From the gas sensing tests, the highest sensing performance was obtained by the 1 at% Ni–ZnO, and then the 0.5 at% Ni–ZnO and 2 at% Ni–ZnO samples. The gas sensing results coincided with the inference of the Ni^{3+}/Ni^{2+} ratio.

5. Conclusions

In summary, different Ni–ZnO core-shell spheres were successfully prepared by a one-step solvothermal method and gas sensors based on the prepared materials were prepared. The role of Ni doping in ZnO on the microstructure and gas sensing performance was studied in detail. The results showed that Ni doping changed the hierarchical microstructure of ZnO, and the BET specific area increased after Ni doping. Gas sensing measurements revealed that the operating temperature decreased due to the lower band gap after Ni doping. All of the sensing materials had the highest response to toluene, the best sensing performance was acquired by the 1 at% Ni–ZnO based gas sensor, with high response, excellent selectivity, fast response and recovery time, and relatively long-term stability. The enhanced sensing property can be mainly due to the increase in the specific surface area and relative percentage of oxygen vacancy after Ni doping, and more importantly, is the catalyst effect of Ni ions. This work provides a reasonable way to fabricate a high performance toluene sensing material.

Supplementary Materials: The following supporting information can be downloaded at: https://www.mdpi.com/article/10.3390/chemosensors10080327/s1, Figure S1: The schematic figure of the (a) ceramic tube, (b) sensor device, and (c) the sensing test system. Figure S2: (a) The UV–Vis absorption spectrum and (b) energy band gap of the ZnO samples with different Ni doping amounts. Table S1: The parameter information for all of the gas samples.

References

1. Mirzaei, A.; Leonardi, S.G.; Neri, G. Detection of hazardous volatile organic compounds (VOCs) by metal oxide nanostructures-based gas sensors: A review. *Ceram. Int.* **2016**, *42*, 15119–15141. [CrossRef]
2. Xu, J.M.; Cheng, J.P. The advances of Co_3O_4 as gas sensing materials: A review. *J. Alloys Compd.* **2016**, *686*, 753–768. [CrossRef]
3. Sharma, B.; Sharma, A.; Joshi, M.; Myung, J.H. Sputtered SnO_2/ZnO heterostructures for improved NO_2 gas sensing properties. *Chemosensors* **2020**, *8*, 67. [CrossRef]
4. Hui, G.Z.; Zhu, M.Y.; Yang, X.L.; Liu, J.J.; Pan, G.F.; Wang, Z.Y. Highly sensitive ethanol gas sensor based on CeO_2/ZnO binary heterojunction composite. *Mater. Lett.* **2020**, *278*, 128453. [CrossRef]
5. Guo, L.L.; Zhang, B.; Yang, X.L.; Zhang, S.S.; Wang, Y.; Wang, G.D. Sensing platform of PdO-ZnO-In_2O_3 nanofibers using MOF templated catalysts for triethylamine detection. *Sens. Actuators B* **2021**, *343*, 130126. [CrossRef]
6. Li, S.H.; Xie, L.L.; He, M.; Hu, X.B.; Luo, G.F.; Chen, C.; Zhu, Z. Metal-Organic frameworks-derived bamboo-like CuO/In_2O_3 Heterostructure for high-performance H_2S gas sensor with Low operating temperature. *Sens. Actuators B* **2020**, *310*, 127828. [CrossRef]
7. Ueda, T.; Boehme, I.; Hyodo, T.; Shimizu, Y.; Weimar, U.; Barsan, N. Enhanced NO_2 sensing properties of Au-loaded porous In_2O_3 gas sensors at low operating temperatures. *Chemosensors* **2020**, *8*, 72. [CrossRef]
8. Yang, X.L.; Zhang, S.F.; Yu, Q.; Zhao, L.P.; Sun, P.; Wang, T.S.; Liu, F.; Yan, X.; Gao, Y.; Liang, X.; et al. One step synthesis of branched SnO_2/ZnO heterostructures and their enhanced gas-sensing properties. *Sens. Actuators B* **2019**, *281*, 415–423. [CrossRef]
9. Hiyoto, K.A.M.; Fisher, E.R. Utilizing plasma modified SnO_2 paper gas sensors to better understand gas-surface interactions at low temperatures. *J. Vac. Sci. Technol. A* **2020**, *38*, 043202. [CrossRef]
10. Zheng, L.; Bi, W.J.; Jin, Z.; Liu, S.T. Synthesis of hierarchical shell-core SnO_2 microspheres and their gas sensing properties. *Chin. Chem. Lett.* **2020**, *31*, 2083–2086. [CrossRef]
11. Ueda, T.; Maeda, T.; Huang, Z.D.; Higuchi, K.; Izawa, K.; Kamada, K.; Hyodo, T.; Shimizu, Y. Enhancement of methylmercaptan sensing response of WO_3 semiconductor gas sensors by gas reactivity and gas diffusivity. *Sens. Actuators B* **2018**, *273*, 826–833. [CrossRef]
12. Buyukkose, S. Highly selective and sensitive WO_3 nanoflakes based ammonia sensor. *Mater. Sci. Semicond. Process.* **2020**, *110*, 104969. [CrossRef]
13. Wang, C.Y.; Li, Y.H.; Qiu, P.P.; Duan, L.L.; Bi, W.; Chen, Y.; Guo, D.; Liu, Y.; Luo, W.; Deng, Y. Controllable synthesis of highly crystallized mesoporous TiO_2/WO_3 heterojunctions for acetone gas sensing. *Chin. Chem. Lett.* **2020**, *31*, 1119–1123. [CrossRef]
14. Mokoena, T.P.; Tshabalala, Z.P.; Hillie, K.T.; Swart, H.C.; Motaung, D.E. The blue luminescence of p-type NiO nanostructured material induced by defects: H_2S gas sensing characteristics at a relatively low operating temperature. *Appl. Surf. Sci.* **2020**, *525*, 146002. [CrossRef]
15. Simion, C.E.; Ghica, C.; Mihalcea, C.G.; Ghica, D.; Mercioniu, I.; Somacescu, S.; Florea, Q.G.; Stanoiu, A. Insights about CO gas-sensing mechanism with NiO-based gas sensors the influence of humidity. *Chemosensors* **2021**, *9*, 244. [CrossRef]
16. Alev, O.; Sarica, N.; Ozdemir, O.; Arslan, L.C.; Buyukkose, S.; Oztur, Z.Z. Cu-doped ZnO nanorods based QCM sensor for hazardous gases. *J. Alloys Compd.* **2020**, *826*, 154177. [CrossRef]
17. Umar, A.; Algadi, H.; Kumar, R.; Akhtar, M.S.; Ibrahim, A.A.; Albargi, H.; Alhamami, M.A.M.; Alsuwian, T.; Zeng, W. Ultrathin leaf-shaped CuO nanosheets based sensor device for enhanced hydrogen sulfide gas sensing application. *Chemosensors* **2021**, *9*, 221. [CrossRef]
18. Reynolds, D.C.; Look, D.C.; Jogai, B.; Hoelscher, J.E.; Sherriff, R.E.; Harris, M.T.; Callahan, M.J. Time-resolved photoluminescence lifetime measurements of the Γ_5 and Γ_6 free excitons in ZnO. *J. Appl. Phys.* **2000**, *88*, 2152–2153. [CrossRef]

19. Norton, D.P.; Heo, Y.W.; Ivill, M.P.; Ip, K.; Pearton, S.J.; Chisholm, M.F. ZnO: Growth, doping & processing. *Mater. Today* **2004**, *7*, 34–40.

20. Modaberi, M.R.; Rooydell, R.; Brahma, S.; Akande, A.A.; Mwakikunga, B.W.; Liu, C.P. Enhanced response and selectivity of H$_2$S sensing through controlled Ni doping into ZnO nanorods by using single metal organic precursors. *Sens. Acuators B* **2018**, *273*, 1278–1290. [CrossRef]

21. Liang, Y.C.; Liao, W.K.; Deng, X.S. Synthesis and substantially enhanced gas sensing sensitivity of homogeneously nanoscale Pd- and Au-particle decorated ZnO nanostructures. *J. Alloys Compd.* **2014**, *599*, 87–92. [CrossRef]

22. Gardon, M.; Guilemany, J.M. A review on fabrication, sensing mechanisms and performance of metal oxide gas sensors. *J. Mater. Sci. Mater. Electron.* **2013**, *24*, 1410–1421. [CrossRef]

23. Hu, J.; Gao, F.Q.; Sang, S.B.; Li, P.W.; Deng, X.; Zhang, W.D.; Chen, Y.; Lian, K. Optimization of Pd content in ZnO microstructures for high-performance gas detection. *J. Mater. Sci.* **2015**, *50*, 1935–1942. [CrossRef]

24. Wang, W.C.; Tian, Y.T.; Wang, X.C.; He, H.; Xu, Y.R.; He, C.; Li, H. Ethanol sensing properties of porous ZnO spheres via hydrothermal route. *J. Mater. Sci.* **2013**, *48*, 3232–3238. [CrossRef]

25. Khoang, N.D.; Hong, H.S.; Trung, D.D.; van Duy, N.; Hoa, N.D.; Thinh, D.D.; Van Hieu, N. On-chip growth of wafer-scale planar-type ZnO nanorod sensors for effective detection of CO gas. *Sens. Actuators B* **2013**, *181*, 529–536. [CrossRef]

26. Zhang, W.H.; Zhang, W.D.; Zhou, J.F. Solvent thermal synthesis and gas-sensing properties of Fe-doped ZnO. *J. Mater. Sci.* **2010**, *45*, 209–215. [CrossRef]

27. Luo, J.; Ma, S.Y.; Li, F.M.; Li, X.B.; Li, W.Q.; Cheng, L.; Mao, Y.Z.; Gz, D.J. The mesoscopic structure of flower-like ZnO nanorods for acetone detection. *Mater. Lett.* **2014**, *121*, 137–140. [CrossRef]

28. Xiong, H.M. ZnO nanoparticles applied to bioimaging and drug delivery. *Adv. Mater.* **2013**, *25*, 5329–5335. [CrossRef]

29. Huang, J.R.; Xu, X.J.; Gu, C.P.; Yang, M.; Yang, M.; Liu, J.H. Large-scale synthesis of hydrated tungsten oxide 3D architectures by a simple chemical solution route and their gas-sensing properties. *J. Mater. Chem.* **2011**, *21*, 13283–13289. [CrossRef]

30. Li, H.Y.; Wang, X. Three-dimensional architectures constructed using two-dimensional nanosheets. *Sci. China Chem.* **2015**, *58*, 1792–1799. [CrossRef]

31. Sohila, S.; Rajendran, R.; Yaakob, Z.; Teridi, M.A.M.; Sopian, K. Photoelectrochemical water splitting performance of flower like ZnO nanostructures synthesized by a novel chemical method. *J. Mater. Sci. Mater. Electron.* **2016**, *27*, 2846–2851. [CrossRef]

32. Akamatsu, T.; Itoh, T.; Tsuruta, A.; Masuda, Y. CH$_3$SH and H$_2$S Sensing Properties of V$_2$O$_5$/WO$_3$/TiO$_2$ Gas Sensor. *Chemosensors* **2021**, *9*, 113. [CrossRef]

33. Li, Y.M.; Hu, H.J.; Zhang, W.F.; Tian, Z.Q.; Jiang, X.Q.; Wang, Y.H.; Zhang, S.; Zhang, Q.; Jian, J.; Zou, J. Theoretical Study on the Electrochemical Catalytic Activity of Au-Doped Pt Electrode for Nitrogen Monoxide. *Chemosensors* **2022**, *10*, 178. [CrossRef]

34. Guo, W.W.; Jian, L.J.; Wang, X.M.; Zeng, W. Hydrothermal synthesis of Ni-doped hydrangea-like Bi$_2$WO$_6$ and the enhanced gas sensing property to n-butanol. *Sens. Actuators B* **2022**, *357*, 131396. [CrossRef]

35. Sun, Q.H.; Wu, Z.F.; Cao, B.B.; Chen, X.; Zhang, C.C.; Shaymurat, T.; Duan, H.; Zhang, J.; Zhang, M. Gas sensing performance of biomass carbon materials promoted by nitrogen doping and p-n junction. *Appl. Surf. Sci.* **2022**, *592*, 153254. [CrossRef]

36. Park, H.; Kim, D.H.; Ma, B.S.; Shin, E.; Kim, Y.; Kim, T.S.; Kim, F.S.; Kim, I.D.; Kim, B.J. High-Performance, Flexible NO$_2$ Chemiresistors Achieved by Design of Imine-Incorporated n-Type Conjugated Polymers. *Adv. Sci.* **2022**, *9*, 2200270. [CrossRef]

37. Fan, Y.R.; Xu, Y.Y.; Wang, Y.X.; Sun, Y.Q. Fabrication and characterization of Co-doped ZnO nanodiscs for selective TEA sensor applications with high response, high selectivity and ppb-level detection limit. *J. Alloys Compd.* **2021**, *876*, 160170. [CrossRef]

38. Lu, S.H.; Hu, X.F.; Zheng, H.; Qiu, J.W.; Tian, R.B.; Quan, W.J.; Min, X.; Ji, P.; Hu, Y.; Cheng, S.; et al. Highly selective, ppb-level xylene gas detection by Sn^{2+}-doped NiO flower-like microspheres prepared by a one-step hydrothermal. *Method Sens.* **2019**, *19*, 2958. [CrossRef]

39. Lee, C.S.; Li, H.Y.; Kim, B.Y.; Jo, Y.M.; Byun, H.G.; Hwang, I.S.; Abdel-Hady, F.; Wazzan, A.A.; Lee, J.-H. Discriminative detection of indoor volatile organic compounds using a sensor array based on pure and Fe-doped In$_2$O$_3$ nanofibers. *Sens. Actuators B* **2019**, *285*, 193–200. [CrossRef]

40. Chacko, L.; Massera, E.; Aneesh, P.M. Enhancement in the selectivity and sensitivity of Ni and Pd functionalized MoS$_2$ toxic gas sensors. *J. Electrochem. Soc.* **2020**, *167*, 106506. [CrossRef]

41. Guo, W.W.; Zhao, B.Y.; Zhou, Q.L.; He, Y.Z.; Wang, Z.C.; Radacsi, N. Fe-doped ZnO/reduced graphene oxide nanocomposite with synergic enhanced gas sensing performance for the effective detection of formaldehyde. *ACS Omega* **2019**, *4*, 10252–10262. [CrossRef]

42. Lu, Y.Y.; Zhan, W.W.; He, Y.; Wang, Y.T.; Kong, X.J.; Kuang, Q.; Xie, Z.; Zheng, X. MOF-templated synthesis of porous Co$_3$O$_4$ concave nanocubes with high specific surface area and their gas sensing properties. *ACS Appl. Mater. Interfaces* **2014**, *6*, 4186–4195. [CrossRef]

43. Li, D.P.; Zhang, Y.; Xu, J.C.; Jin, H.X.; Jin, D.F.; Hong, B.; Peng, X.; Wang, P.; Ge, H.; Wang, X. Nanocasting synthesis and gas-sensing behavior of hematite nanowires. *Phys. E Low-Dimens. Syst. Nanostruct. (Amst. Neth.)* **2016**, *84*, 395–400. [CrossRef]

44. Chen, H.D.; Jin, K.L.; Wang, P.F.; Xu, J.C.; Han, Y.B.; Jin, H.X.; Jin, D.F.; Peng, X.L.; Hong, B.; Li, J.; et al. Highly enhanced gas-sensing properties of indium-doped mesoporous hematite nanowires. *J. Phys. Chem. Solids* **2018**, *120*, 271–278. [CrossRef]

45. Su, C.; Zhang, L.; Han, Y.T.; Ren, C.; Li, B.L.; Wang, T.; Zeng, M.; Su, Y.; Hu, N.; Zhou, Z.; et al. Glucose-assisted synthesis of hierarchical NiO-ZnO heterostructure with enhanced glycol gas sensing performance. *Sens. Actuators B* **2021**, *329*, 129167. [CrossRef]

46. Sun, K.; Zhan, G.H.; Chen, H.D.; Lin, S.W. Low-operating-temperature NO$_2$ sensor based on a CeO$_2$/ZnO heterojunction. *Sensors* **2021**, *21*, 8269. [CrossRef] [PubMed]

47. Zhao, Y.M.; Wang, S.; Zhai, X.; Shao, L.; Bai, X.J.; Liu, Y.L.; Wang, T.; Li, Y.; Zhang, L.; Fan, F.; et al. Construction of Zn/Ni bimetallic organic framework derived ZnO/NiO heterostructure with superior N-propanol sensing performance. *ACS Appl. Mater. Interfaces* **2021**, *13*, 9206–9215. [CrossRef] [PubMed]

48. Duan, Z.H.; Zhao, Q.N.; Wang, S.; Huang, Q.; Yuan, Z.; Zhang, Y.J.; Jiang, Y.; Tai, H. Halloysite nanotubes: Natural, environmental-friendly and low-cost nanomaterials for high-performance humidity sensor. *Sens. Actuators B* **2020**, *317*, 128204. [CrossRef]

49. Chen, X.X.; Shen, Y.B.; Zhou, P.F.; Zhong, X.X.; Li, G.D.; Han, C.; Wei, D.; Li, S. Bimetallic Au/Pd nanoparticles decorated ZnO nanowires for NO$_2$ detection. *Sens. Actuators B* **2019**, *289*, 160–168. [CrossRef]

50. Zhou, C.G.; Meng, F.Q.; Chen, K.; Yang, X.L.; Wang, T.S.; Sun, P.; Liu, F.; Yan, X.; Shimanoe, K.; Lu, G. High sensitivity and low detection limit of acetone sensor based on NiO/Zn$_2$SnO$_4$ p-n heterojunction octahedrons. *Sens. Actuators B* **2021**, *339*, 129912. [CrossRef]

51. Wang, C.; Cui, X.B.; Liu, J.Y.; Zhou, X.; Cheng, X.Y.; Sun, P.; Hu, X.; Li, X.; Zheng, J.; Lu, G. Design of superior ethanol gas sensor based on Al-doped NiO nanorod-flowers. *ACS Sens.* **2016**, *1*, 131–136. [CrossRef]

52. Wang, S.; Huang, D.; Xu, S.S.; Jiang, W.K.; Wang, T.; Hu, J.; Hu, N.; Su, Y.; Zhang, Y.; Yang, Z. Two-dimensional NiO nanosheets with enhanced room temperature NO$_2$ sensing performance via Al doping. *Phys. Chem. Chem. Phys.* **2017**, *19*, 19043–19049. [CrossRef]

53. Wang, L.L.; Lou, Z.; Zhang, R.; Zhou, T.T.; Deng, J.N.; Zhang, T. Hybrid Co3O$_4$/SnO$_2$ core-shell nanospheres as real-time rapid-response sensors for ammonia gas. *ACS Appl. Mater. Interfaces* **2016**, *8*, 6539–6545. [CrossRef]

54. Korotcenkov, G.; Cho, B.K. Engineering approaches for the improvement of conductometric gas sensor parameters Part 1. Improvement of sensor sensitivity and selectivity (short survey). *Sens. Actuators B* **2013**, *188*, 709–728. [CrossRef]

55. Li, F.; Gao, X.; Wang, R.; Zhang, T. Design of WO$_3$-SnO$_2$ core-shell nanofibers and their enhanced gas sensing performance based on different work function. *Appl. Surf. Sci.* **2018**, *442*, 30–37. [CrossRef]

56. Kim, J.H.; Kim, H.W.; Kim, S.S. Self-heating effects on the toluene sensing of Pt-functionalized SnO$_2$-ZnO core-shell nanowires. *Sens. Actuators B* **2017**, *251*, 781–794. [CrossRef]

57. Chen, H.; Ao, S.R.; Li, G.D.; Gao, Q.; Zou, X.X.; Wei, C.D. Enhanced sensing performance to toluene and xylene by constructing NiGa$_2$O$_4$-NiO heterostructures. *Sens. Actuators B* **2019**, *282*, 331–338. [CrossRef]

58. Nie, L.F.; Fan, G.J.; Wang, A.Q.; Zhang, L.; Guan, J.; Han, N.; Chen, Y. Finely dispersed and highly toluene sensitive NiO/NiGa$_2$O$_4$ heterostructures prepared from layered double hydroxides precursors. *Sens. Actuators B* **2021**, *345*, 130412. [CrossRef]

59. Hermawan, A.; Asakura, Y.; Inada, M.; Yin, S. A facile method for preparation of uniformly decorated-spherical SnO$_2$ by CuO nanoparticles for highly responsive toluene detection at high temperature. *J. Mater. Sci. Technol.* **2020**, *51*, 119–129. [CrossRef]

60. Jamnik, D.J.S.S.I. Investigation of the PTCR effect in ZnO–NiO two-phase ceramics. *Solid State Ion.* **1997**, *99*, 125–135.

61. Kim, H.J.; Lee, J.H. Highly sensitive and selective gas sensors using p-type oxide semiconductors: Overview. *Sens. Actuators B* **2014**, *192*, 607–627. [CrossRef]

62. Jun, J.H.; Yun, J.; Cho, K.; Hwang, I.S.; Lee, J.H.; Kim, S. Necked ZnO nanoparticle-based NO$_2$ sensors with high and fast response. *Sens. Actuators B* **2009**, *140*, 412–417. [CrossRef]

63. Zhou, J.Y.; Bai, J.L.; Zhao, H.; Yang, Z.Y.; Gu, X.Y.; Huang, B.Y.; Zhao, C.H.; Cairang, L.; Sun, G.Z.; Zhang, Z.X.; et al. Gas sensing enhancing mechanism via doping-induced oxygen vacancies for gas sensors based on indium tin oxide nanotubes. *Sens. Actuators B* **2018**, *265*, 273–284. [CrossRef]

64. Patil, V.L.; Vanalakar, S.A.; Patil, P.S.; Kim, J.H. Fabrication of nanostructured ZnO thin films based NO$_2$ gas sensor via SILAR technique. *Sens. Actuators B* **2017**, *239*, 1185–1193. [CrossRef]

65. Zhang, R.; Gao, S.; Zhou, T.T.; Tu, J.C.; Zhang, T. Facile preparation of hierarchical structure based on p-type Co$_3$O$_4$ as toluene detecting sensor. *Appl. Surf. Sci.* **2020**, *503*, 144167. [CrossRef]

66. Zhang, R.; Xu, Z.W.; Zhou, T.T.; Fei, T.; Wang, R.; Zhang, T. Improvement of gas sensing performance for tin dioxide sensor through construction of nanostructures. *JCIS* **2019**, *557*, 673–682. [CrossRef]

67. Kim, J.H.; Mirzaei, A.; Kim, H.W.; Kim, S.S. Variation of shell thickness in ZnO-SnO$_2$ core-shell nanowires for optimizing sensing behaviors to CO, C6H6, and C7H8 gases. *Sens. Actuators B* **2020**, *302*, 127150. [CrossRef]

68. Bai, J.L.; Zhao, C.H.; Gong, H.M.; Wang, Q.; Huang, B.Y.; Sun, G.Z.; Wang, Y.; Zhou, J.; Xie, E.; Wang, F. Debye-length controlled gas sensing performances in NiO@ZnO p-n junctional core-shell nanotubes. *J. Phys. D Appl. Phys.* **2019**, *52*, 285103. [CrossRef]

69. Zhou, T.T.; Zhang, T.; Zeng, Y.; Zhang, R.; Lou, Z.; Deng, J.N.; Wang, L. Structure-driven efficient NiFe$_2$O$_4$ materials for ultra-fast response electronic sensing platform. *Sens. Actuators B* **2018**, *255*, 1436–1444. [CrossRef]

70. Kim, H.R.; Choi, K.I.; Kim, K.M.; Kim, I.D.; Cao, G.Z.; Lee, J.H. Ultra-fast responding and recovering C$_2$H$_5$OH sensors using SnO$_2$ hollow spheres prepared and activated by Ni templates. *Chem. Commun.* **2010**, *46*, 5061–5063. [CrossRef]

71. Yang, M.; Lu, J.Y.; Wang, X.; Zhang, H.; Chen, F.; Sun, J.B.; Yang, J.; Sun, Y.; Lu, G. Acetone sensors with high stability to humidity changes based on Ru-doped NiO flower-like microspheres. *Sens. Actuators B* **2020**, *313*, 127965. [CrossRef]

72. Luo, Y.B.; An, B.X.; Bai, J.L.; Wang, Y.R.; Cheng, X.; Wang, Q.; Li, J.; Yang, Y.; Wu, Z.; Xie, E. Ultrahigh-response hydrogen sensor based on PdO/NiO co-doped In$_2$O$_3$ nanotubes. *J. Colloid Interface Sci.* **2021**, *599*, 533–542. [CrossRef]